Development of Super-resolution Sharpness-based Axial Localization for Ultrasound Imaging

This article has been accepted for publication in a future issue of this journal, but has not been fully edited. Content may change prior to final publication. Citation information: DOI 10.1109/ACCESS.2018.2889425, IEEE Access

Development of Super-resolution Sharpness-based Axial Localization for Ultrasound Imaging

Konstantinos Diamantis, Tom Anderson, Jørgen Arendt Jensen, *Fellow, IEEE,*
Paul A. Dalgarno, and Vassilis Sboros

***Abstract*—Super-resolution ultrasound mostly uses image-based methods for the localization of single scatterers. These methods are largely based on the centre of mass (COM) calculation. Sharpness-based localization is an alternative to COM for scatterer localization in the axial direction. Simulated ultrasound point scatterer data (centre frequency $f_0 = 7$ MHz, wavelength $\lambda = 220$ μm) showed that the normalized sharpness method can provide scatterer axial localization with an accuracy down to 2 μm ($< 0.01\lambda$), which is a two-order of magnitude improvement compared to that achievable by conventional imaging ($\approx \lambda$), and a 5-fold improvement compared to the COM estimate ($\approx$10 μm or 0.05λ). Similar results were obtained experimentally using wire-target data acquired by the Synthetic Aperture Real-time Ultrasound System (SARUS). The performance of the proposed method was also found to be consistent across different types of ultrasound transmission. The localization precision deteriorates in the presence of noise, but even in very low signal-to-noise-ratio (SNR = 0 dB) the uncertainty was not higher than 6 μm, which outperforms the COM estimate. The method can be implemented in image data as well as using the raw signals. It is proposed that signal derived localization should replace the image-based equivalent, as it provides at least a 10 times improved accuracy.**

***Index Terms*—Axial localization, centre of mass, multiple focusing, normalized sharpness, super-resolution ultrasound**

I. Introduction

SINGLE ultrasound contrast microbubbles (MBs) provide adequate signal-to-noise-ratio (SNR) and thus can be tracked as they travel through the vascular bed. The particle tracking approaches employed in super-resolution ultrasound imaging are similar to localization microscopy [1]–[3] resulting in super-resolved paths, that provide images beyond the diffraction limit, which is comparable to the wavelength (λ). In this way it was possible to obtain high resolution transcranial images of vascular structure [4], [5], and to achieve *in-vivo* imaging of the mouse ear microvasculature [6], and of ≤ 10 μm-diameter rodent cerebral microvessels [7]–[9]. Most super-resolution results were acquired using methods that mainly depend on images and image processing, with the exception of [10], [11] where the studies were driven by a theoretical localization precision limit ($\lambda/38$) calculated for the particular ultrasound system. Thus, little is implemented to overcome the inherent limitations of the ultrasound spatial resolution. Commonly the images used, result from standard processing of the signals received by the transducer and do not prioritize the enhancement of point scatterer imaging. The waveform, beam-formation, gain, compression, interpolation and display algorithms used, can be viewed as steps that aim to enhance images of structural content, such as anatomy, but also reduce and modify signal information that is difficult to recover [12], [13]. Therefore, there is potential to combine the raw signal information with advanced signal processing techniques to achieve greater precision in particle localization.

The use of multi-focal imaging combined with the simple metric of sharpness is a different approach to obtain axial localization in the micrometre range [14], and it can be implemented either in image or raw ultrasound data. It was demonstrated that plane wave (PW) transmissions of ultrasound, and the use of 3 receive foci at 2 mm separation provided an axial localization precision of 10.21 μm (or $\lambda/21$) with SNR $= 10$ dB. These results were obtained from individual point-spread-functions (PSFs), where the PSF is the ultrasound system's response to a single point scatterer. The experiments were performed in ideal imaging conditions and the impact of the type of ultrasound transmission was not assessed. This proof of principle experiment used unfocused (PW) transmission [15] as it is the best approximation to the unfocused light transmission, which was implemented in the original presentation of the method in optical microscopy [16], [17]. Although this facilitates fast acquisitions as only one emission is able to provide all the necessary data for the method, the acoustic pressure drops significantly with depth, thus limiting the depth of the imaging region, and potentially generating variable MB detection sensitivity across the image. This is due to the combination of the dependence of the MB scattering cross section on acoustic pressure, and the effect of acoustic pressure on MB destruction [18], [19]. Focused ultrasound requires several emissions that are all used to form one image and thus lowers the achievable frame rate. However, it has the potential to provide the least variable ultrasound field, which may provide a relatively even MB density across the image. This is therefore a candidate option for generating super-resolution images of large organs. The choice of optimal ultrasound transmission may impact on the performance of the sharpness-based axial localization, and as

This work was supported by the Science and Technology Facilities Council (STFC-ST/M007804/1), by grant 82-2012-4 from the Danish Advanced Technology Foundation, and by B-K Medical ApS. *Asterisk indicates corresponding author.*

K. Diamantis is with the School of Engineering, Institute for Digital Communications (IDCOM), The University of Edinburgh, UK.

T. Anderson is with the School of Clinical Sciences, Centre of Cardiovascular Science, The University of Edinburgh, UK.

J. A. Jensen is with the Department of Electrical Engineering, Center for Fast Ultrasound Imaging, Technical University of Denmark, Kgs. Lyngby, Denmark.

P. A. Dalgarno, and *V. Sboros (e-mail: V.Sboros@hw.ac.uk) are with the Institute of Biological Chemistry, Biophysics and Bioengineering (IB3), Heriot-Watt (HW) University, Edinburgh, UK.

This article has been accepted for publication in a future issue of this journal, but has not been fully edited. Content may change prior to final publication. Citation information: DOI 10.1109/ACCESS.2018.2889425, IEEE Access

a consequence it is important to assess the method's accuracy for different transmission protocols. Furthermore, the impact of SNR on localization accuracy needs to be investigated to explore the potential of the technique under more realistic imaging conditions. Finally, the optimization process requires an understanding of the role of the foci spacing, that is directly related to the sampling of the method.

The purpose of the present article is threefold. First, this study aims to further develop the sharpness method that was initially presented in [14], by investigating all the parameters described above (varying foci spacing during the receive processing, varying SNR and ultrasound transmissions). The second objective is to investigate imaging regions that may provide improved axial localization, and to identify an optimal combination between high accuracy and imaging region of substantial length for which this accuracy is maintained, as it appears to be a trade-off between the two. All findings of the sharpness-based axial localization are then compared with these obtained using the centre of mass (COM), which is the tool mainly employed by current super-resolution ultrasound methods in order to determine scatterer location. Third, given that the sharpness method relies on good quality calibration data, an important part of the analysis focuses on the possibility to extract a reliable estimation of the method's uncertainty that will provide the prospect for developing the method to perform well without calibration data. Methodologically, all these are accomplished using Field II [20], [21] simulated ultrasound point scatterer data and a simple experimental wire-target phantom to confirm the simulations.

II. Methods

A. Sharpness-based Localization

The method is directly translated from cellular microscopy [16], [17] and is based on multi-focal imaging and the simple, aberration dependent, image sharpness metric of a single point scatterer [22]–[24]. The localization of a point scatterer relies on the generation of multiple overlapping sharpness curves (*S*-curves), which describe the inherent behaviour of a scatterer through the axial range, created by deploying multiple foci during receive processing, and by assessing the sharpness values after each acquisition as a function of depth [14], [25], [26]. Each derived *S*-curve peaks around the receive focus. The unique position of the scatterer is identified by combining a calibration standard with a maximum likelihood (ML) estimator for the sharpness data probability density function (PDF). The latter is a Gamma distribution that shows the probability of measuring a specific sharpness value from point scatterer data at a specific depth and using a specific receive focus. The calibration data consist of reference *S*-curves, generated by performing well-controlled repetitive sharpness measurements, during which the point scatterer's position is always known. An outline of the method which was used for axial localization of isolated ultrasound point scatterers is shown in Algorithm 1 and more information can be found in [14]. Briefly, the ultrasound reflection of a scatterer at a specific depth in the field is acquired, and this is repeated for a selected depth (z) range. The raw ultrasound data are then beamformed offline using the standard Delay-And-Sum (DAS) beamformer and fixed receive focusing. A normalized version of sharpness (S) is adopted in this work and is defined as follows:

$$S = \begin{cases} \dfrac{\sum_{k=1}^{K} n_k^2}{(\sum_{k=1}^{K} n_k)^2}, \text{ using pixel intensity } (S_{int}), \\ \\ \dfrac{\sum_{q=1}^{Q} |E_q|^4}{(\sum_{q=1}^{Q} |E_q|^2)^2}, \text{ using signal envelope } (S_{env}), \end{cases}$$

where the denominator corresponds to the normalization factor in both cases. A single S_{int} value is calculated from a small square area including the PSF main-lobe and consisting of K square pixels with n_k recorded image pixel intensities ($k = 1, \ldots, K$). Similarly, a single S_{env} value is calculated from the same square area represented by Q envelope detected signal samples with amplitude $|E_q|$ ($q = 1, \ldots, Q$). There is no correlation between K and Q as the former depends solely on the image format and the latter on the number of transducer elements and on the frequency that the data are sampled. As the pixel intensities are proportional to the squared signal amplitudes, 4^{th}-order statistics appear in the S_{env} formulation. A number of sharpness values (either S_{int} or S_{env}) as measured from a single data acquisition of an isolated point scatterer can provide a depth position estimate, which is the PDF peak, with reduced uncertainty compared to that achievable by conventional ultrasound.

Algorithm 1 Sharpness-based axial scatterer localization

for $z = z_{start}$ to z_{end} **do**
  Create phantom with a point scatterer at depth z
  for $i = 1$ to v **do**
    Emit wave i from the active aperture
    Collect and store raw ultrasound data
    for $j = 1$ to 3 **do**
      Beamform data with fixed focus j in receive
    end for
  end for
end for
if signal-derived sharpness $= true$ **then**
  Calculate all S_{env} sharpness values for each z, i, j
else
  Calculate all S_{int} sharpness values for each z, i, j
end if
Calculate statistical measures from sharpness data
  Extract mean sharpness values for each position
  Extract the standard deviation (SD) from mean values
Plot mean S-values and associated deviation over depth
Interpolate the sharpness data by a K_{interp} factor
Apply the ML estimator to the interpolated data
Estimate the depth position (PDF peak value)
Compare the depth estimate with true scatterer position

This article has been accepted for publication in a future issue of this journal, but has not been fully edited. Content may change prior to final publication. Citation information: DOI 10.1109/ACCESS.2018.2889425, IEEE Access

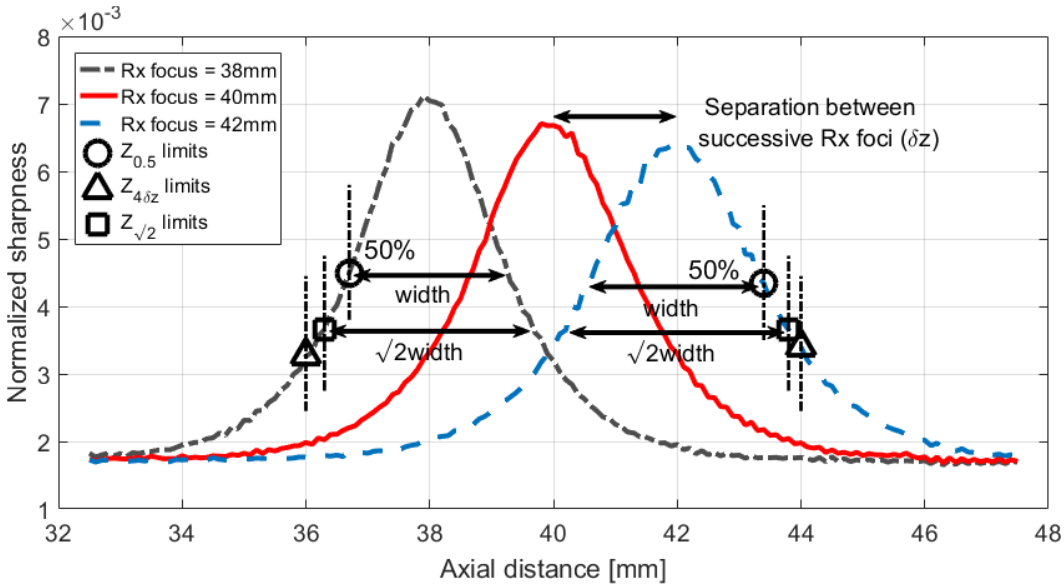

Fig. 1. An example set of three mean *S*-curves plotted over depth. The sharpness data were created using PW ultrasound transmission. The two circles indicate the sharpness values that correspond to 50% *S*-curve amplitude of the extreme *S*-curves ($Z_{0.5}$ limits). The two triangles correspond to the distance that is equal to 2 times the separation between successive receive foci either way of the central focus ($Z_{4\delta_z}$ limits). The two squares indicate the sharpness values that correspond to $\sqrt{2}$-times the width of the extreme *S*-curves ($Z_{\sqrt{2}}$ limits).

B. Data Analysis

The accuracy of the normalized sharpness method is assessed by the depth deviation d_{dev} of the method's z-estimate to the actual scatterer position, which is known for all simulations and is established from a high precision translation stage in the experiments. For v repetitive measurements and thus v image frames per axial position, d_{dev} results from the root mean square error (RMSE) from all v cases. The sharpness standard deviation (SD) and the full-width-at-half-maximum (FWHM) of the PDF are compared with the d_{dev} values in order to evaluate their dependencies. The average d_{dev} is also calculated for different depth ranges, knowing that the normalized sharpness method does not perform uniformly for the whole range of scatterer axial displacement [14]. The rationale is that the areas with the maximum rate of sharpness change (*S*-curves slopes) are also the areas of highest localization accuracy. For this reason, the *S*-curve edges, where the sharpness values vary little may be ignored for the average d_{dev} calculation. The standard deviation d_{SD}, of the average d_{dev} is the measurement uncertainty. Individual d_{dev} values that are outside the $\pm 2d_{SD}$ limits of the average d_{dev}, are rejected as outliers, using the "trimmean" Matlab (The MathWorks, Inc., Natick, MA, USA) function. Three different depth ranges that can be automatically determined, and can potentially cover a large part of the entire axial displacement have been examined in this work. These can be found in Fig. 1 alongside with a set of three typical *S*-curves generated by employing receive (Rx) foci at 38 mm, 40 mm, and 42 mm.

In Fig. 1, $Z_{0.5}$ is determined as the distance between the two circles that indicate the sharpness values that correspond to 50% *S*-curve amplitude of the extreme *S*-curves. $Z_{4\delta_z}$ is the distance between the two triangles and corresponds to the distance that is equal to 2 times the separation between successive receive foci (δz) either way of the central focus, thus $4\delta z$ in total. Finally, $Z_{\sqrt{2}}$ is defined by the distance between the two squares that indicate the sharpness values that correspond to $\sqrt{2}$-times the width of the extreme *S*-curves. In general, $Z_{0.5}$ and $Z_{\sqrt{2}}$ are adaptive depth ranges that depend on the shape of the *S*-curve, while $Z_{4\delta_z}$ is fixed and defined by the foci separation. There are small differences between the three depth ranges when the foci separation is 2 mm as shown from Fig. 1. However, $Z_{4\delta_z}$ becomes considerably larger than the other two ranges for successive foci separation higher than 3 mm. In the results these ranges are used to compare the axial localization accuracy achieved by signal and image sharpness data as well as with the localization achieved by the use of COM. The COM was calculated for all point scatterer images using the standard "regionprops" Matlab function. The latter is a built-in function of the image processing toolbox that can measure a set of properties for an image region, using the pixel values. The function requires that the images have been binarized using an intensity threshold prior to the any estimation. The process is similar to the one followed in [6]. A 256-color grayscale is conventionally employed and pixel intensities regularly take values between 0 (black) and 255 (white). The binarization converts these values to either 0 or 1 depending on a threshold set by the user. The depth deviation of the COM estimates to the actual scatterer position (d_{dev}) is also used to evaluate the method's performance, for a fair comparison with the sharpness-based axial localization results.

C. Simulation of Point Scatterers

The Field II [20], [21] ultrasound simulation software was used for this study. A phantom consisting of a single point scatterer at a depth of 40 mm, was created and scanned by a 7 MHz, 192 element, linear array simulated transducer with

This article has been accepted for publication in a future issue of this journal, but has not been fully edited. Content may change prior to final publication. Citation information: DOI 10.1109/ACCESS.2018.2889425, IEEE Access

λ spacing. Different types of ultrasound transmission were employed. First, an unfocused PW emission with the central transducer element (#96) located above the point scatterer was implemented. Raw data from one emission were acquired from all 192 channels individually in receive. The data were stored, and the same emission was repeated for 151 axial displacement steps of 100 μm from position 32.5 mm to 47.5 mm. The simulation was repeated 10 times in the presence of noise, and 3 *S*-curves were used to achieve the axial localization. The PW data were used to study the effect of the foci separation and of the image noise in the accuracy of the axial localization using the normalized sharpness method. For each acquisition the data were beamformed with 21 different foci in receive between 35 mm and 45 mm, to examine various foci spacing cases for the 3 S-curves. The use of a central receive focus at a depth of 40 mm, (the scatterer's initial position) and then of two other values at -2 mm and $+2$ mm of the starting depth was deployed for the rest of the simulations. For that case, white Gaussian noise was added to the raw simulated signals, with different SNR values ranging between 0 dB and 30 dB.

Next, the central transducer element was used to emit an unfocused spherical wave, as described in [27]. The repetition of such emissions using different transducer elements as the transmitting aperture, and the combination of the resulting images is the principle of synthetic aperture (SA) ultrasound [28]. Finally, standard focused beams were transmitted using 64 elements as the transmitting aperture and a fixed transmit focus at (a) 30 mm depth which was higher than the scatterer highest depth position, (b) 40 mm depth which was equivalent to the scatterer's initial position, and (c) 50 mm depth which was lower than the lowest scatterer depth position. Each focused transmission involved the creation of 128 scan lines that were combined to form an ultrasound image. The speed of sound, c was set to 1540 m/s and all the parameters for the simulation data are given in Table I.

TABLE I
SIMULATION SCAN PARAMETERS

Parameter Name	Field II Simulations
Transducer type	Linear array
Transducer element pitch	208 μm
Transducer element kerf	35 μm
Transducer element height	4.5 mm
Centre frequency, f_0	7 MHz
Sampling frequency, f_s	100 MHz
Speed of sound, c	1540 m/s
Wavelength, $\lambda = c/f_0$	220 μm
Excitation pulse	Two-cycle sinusoid at f_0
Transmit focus	unfocused/30 mm/40 mm/50 mm
Transmit apodization	Hanning
Number of transmitting elements	1/64/192
Number of emissions per frame	1/128
Fixed receive (Rx) focus	35 mm to 45 mm
Receive apodization	Hanning
Number of receiving elements, M	192
Start depth, z_{start}	32.5 mm
End depth, z_{end}	47.5 mm
Axial distance covered	15 mm
z-step between successive axial positions	100 μm
Number of frames per axial position, v	10
Signal-to-Noise-Ratio, *SNR*	0 dB to 30 dB

D. Wire-target Experiment

A 0.07 mm diameter copper wire inside a water tank, was used to create a custom phantom with movement flexibility. The initial wire position was (x,z)=$(0,40)$ mm. After an ultrasound transmission, the wire was moved to the next z position in the axial direction using the AIMS III positioning setup (Onda Corporation, Sunnyvale, CA, USA), which was controlled using a Matlab interface. Pictures of the phantom and of the entire experimental setup can be found in Fig. 2.

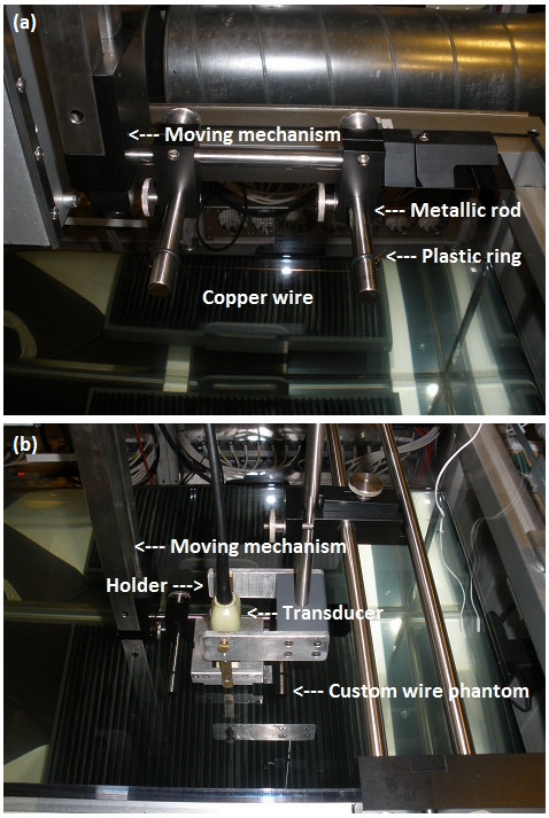

Fig. 2. (a) The custom phantom used for the experiments consisted of a copper wire. The wire was mounted on metal rods attached to a linear stage by means of plastic rings. This arrangement allowed movement of the wire in the axial direction. (b) A linear array transducer was attached to a fixed holder and positioned vertically above the wire-target.

For the experiment, z-steps of 108.7 μm were used as this was dictated by the minimum movement step (10.87 μm). Data were produced across 15 mm, between 32.5 mm and 47.5 mm from the transducer face, thus 139 steps were required. The speed of sound was calculated to $c = 1484$ m/s based on the water temperature [29], and this resulted into a slightly different wavelength (212 μm) compared to the simulations. The measurements were performed by the 1024 channel experimental ultrasound scanner SARUS (Synthetic Aperture Real-time Ultrasound System) [30], and the data were sampled at 35 MHz. The remaining scan parameters were similar to these shown in Table I for the simulation study. The transmission of ultrasound was performed with single plane waves only, where the transmit aperture consisted of all the elements in the array. Raw data from one unfocused emission were acquired from all 192 channels individually in

This article has been accepted for publication in a future issue of this journal, but has not been fully edited. Content may change prior to final publication. Citation information: DOI 10.1109/ACCESS.2018.2889425, IEEE Access

receive. The data acquisition was repeated 10 times for each wire-target position, and the wire was then moved to the next location in the axial direction. For each acquisition the data were beamformed to three different foci in receive with the use of an in-house programmed beamformation toolbox BFT III [31]. The receive foci were placed at 38 mm, 40 mm, and 42 mm.

III. Results: Simulation Study

A. Distance Between Receive Foci

Using a PW transmission, the normalized-sharpness algorithm was implemented for varying distances between receive foci ranging between 0.5 mm and 5 mm with a 0.5 mm step. Fig. 3(a)-(b) shows examples of 3 resulting *S*-curve sets when the foci separation is 1 mm, and 4 mm, respectively. Sharpness values were higher when shorter receive foci (i.e. closer to the transducer's surface) were used with an approximate peak value decrease of $3-5\%$ per mm depth. In addition, the resulting *S*-curves were narrower for the receive foci closer to the transducer, with a $4-7\%$ FWHM increase per mm.

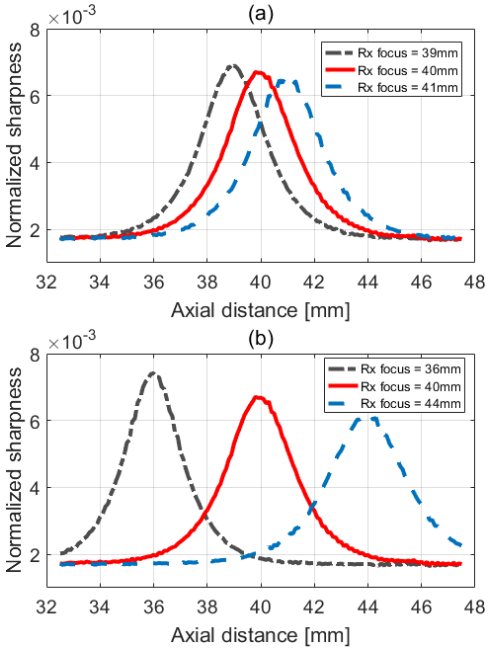

Fig. 3. Normalized sharpness as a function of axial displacement. Two different sets of 3 signal-derived *S*-curves are displayed where the ultrasound data were acquired by unfocused plane wave transmission and the receive processing was performed using a) 1 mm, and b) 4 mm separation between successive fixed receive foci.

The foci separation and the curve shape determine the size of $Z_{0.5}$, $Z_{4\delta z}$, and $Z_{\sqrt{2}}$ and their achievable axial localization accuracy. These are depicted in Fig. 4 for foci separations between 0.5 mm and 5 mm. Overall the 3 depth ranges provided very similar results. $Z_{0.5}$ provided a lowest average d_{dev} equal to 1.43 μm ($< 0.01\lambda$) and its associated standard deviation (d_{SD}) was ± 1.19 μm (Fig. 4(a)). These values were acquired for an 1 mm successive foci separation and maintained for a depth range of 4.9 mm as shown in Fig. 4(b). The average d_{dev} remained below 2 μm (or $\approx 0.01\lambda$) for foci separations below 2 mm and increased for larger separation distances as shown in Fig. 4(a). The highest average d_{dev} for $Z_{0.5}$ was 3.20 ± 2.96 μm, for a 5 mm successive foci separation. $Z_{4\delta z}$ provided an average d_{dev} between 1.50 ± 1.27 μm (1 mm separation) and 3.10 ± 2.92 μm (4.5 mm separation). Finally, $Z_{\sqrt{2}}$ provided an average d_{dev} between 1.44 ± 1.27 μm (1 mm separation) and 3.13 ± 2.90 μm (5 mm separation).

In general, larger foci separation is equivalent to larger sizes for all 3 depth ranges (Fig. 4(b)). $Z_{0.5}$ varied from 3.8 mm (at 0.5 mm foci separation) to 12.9 mm (5 mm separation). $Z_{4\delta z}$ varied from 2 mm to 20 mm. However, sharpness data were generated for a 15 mm axial displacement range (section II-C) and this value was used for the last 3 foci separations (4-5 mm). $Z_{\sqrt{2}}$ was found similar but slightly extended compared to $Z_{0.5}$, ranging between 4.9 mm and 13.8 mm. Note that $Z_{4\delta z}$ is a linear function to foci separation while $Z_{0.5}$ and $Z_{\sqrt{2}}$ depend on the width of the *S*-curve which is not constant (Fig. 3). Moreover, Fig. 4 shows that the 2 mm foci separation provided overall a good combination of low average d_{dev} (1.84 μm or $\approx 0.01\lambda$) and low d_{SD} (± 1.54) for a relatively high depth range ($Z_{0.5} = 6.8$ mm). Thus, this was the selected separation for the remainder of the parametric study, using only the $Z_{0.5}$ distance.

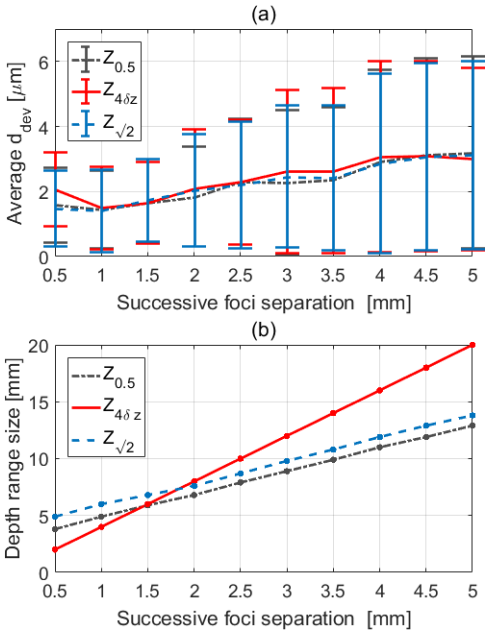

Fig. 4. (a) Average depth deviation to true scatterer position (d_{dev}) for the $Z_{0.5}$, $Z_{4\delta z}$, and $Z_{\sqrt{2}}$ depth ranges, and (b) their sizes over varying distances between successive receive foci positions, using signal-derived sharpness data.

B. Signal-to-Noise-Ratio

Lower SNR values (noisier signals) increase the sharpness SD, and this introduces higher uncertainty in the estimation of the depth position, through the ML estimator. Fig. 5(a)-(d) illustrates how the simulated point scatterer images appear when 4 different SNR values have been employed, 0 dB, 10 dB, 20 dB, and 30 dB respectively, using PW transmission and a receive focus set to 40 mm depth.

This article has been accepted for publication in a future issue of this journal, but has not been fully edited. Content may change prior to final publication. Citation information: DOI 10.1109/ACCESS.2018.2889425, IEEE Access

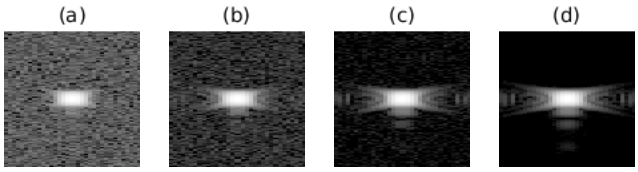

Fig. 5. Four simulated PSFs after adding white Gaussian noise to the raw ultrasound signals, resulting in SNR of a) 0 dB, b) 10 dB, c) 20 dB and, d) 30 dB. The receive focus was set to 40 mm and the scatterer was positioned to 40 mm depth. Each image area is 3.5 mm × 3.5 mm and a 60 dB dynamic range display was used.

In Fig. 6(a) the average d_{dev} is plotted over increasing SNR, and was found as low as 0.15 ± 0.12 μm for SNR $= 30$ dB. This value is more than 3 orders of magnitude lower compared to the used wavelength (220 μm). The average d_{dev} remained below 2 μm for SNR values up to 10 dB and increased for noisier backgrounds to reach a maximum average of 5.29 ± 4.08 μm for SNR$= 0$ dB. Despite this increase, the latter value was equivalent to $\approx 0.02\lambda$. Fig. 6(b) shows how the d_{dev} measured for each depth position relates to the normalized sharpness standard deviation that was measured from the 10 repetitive sharpness measurements as described in section II-B. The scatter plot includes all studied SNRs and confirms that generally a low sharpness SD will be translated into a low d_{dev}. Approximately 71% of the measured d_{dev} values were found below 2 μm and the remaining were associated with the cases of large noise addition. From this 71% of low d_{dev}, only 19% was associated with normalized sharpness standard deviation higher than 2×10^{-5}.

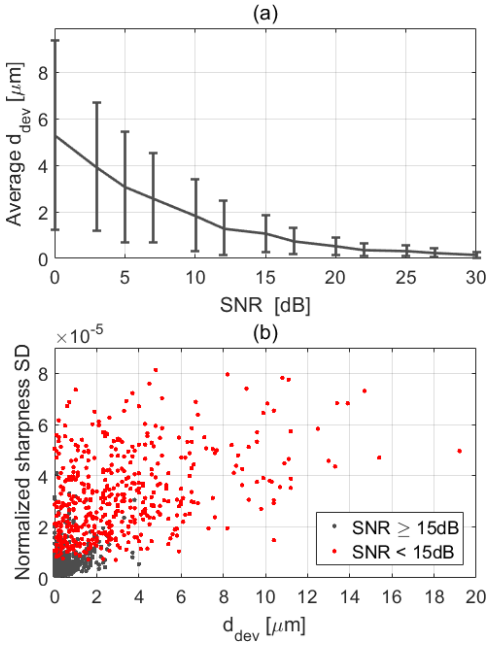

Fig. 6. (a) Average depth deviation to true scatterer position (d_{dev}) over different SNR values added to the raw ultrasound signals, using signal-derived sharpness data, and (b) normalized sharpness standard deviation over individual d_{dev} values for all SNR values used.

C. Transmitting Aperture

The effect of ultrasound transmit aperture on the sharpness calculation and subsequently on axial localization accuracy is displayed on Table II. As shown in the table, the spherical wave provided no significant difference ($< 10\%$) compared to the PW transmission. The *S*-curves were also similar to Fig. 1 (PW transmission). This was expected since both transmission types were unfocused and they do not introduce any focus-related bias term to the calculation of the normalized sharpness. On the other hand, the effect of transmit focus in the next simulations affected the shape of the *S*-curves. Examples of three sets of *S*-curves with transmit foci equal to 30 mm, 40 mm, and 50 mm are displayed in Fig. 7(a),(b), and (c) respectively. Despite the changes in the *S*-curves shape, the accuracy of the axial localization was in the same range with the other transmissions and varied between 1.84 μm and 2.21 μm (Table II).

TABLE II
AVERAGE DEPTH DEVIATION AND ITS STANDARD DEVIATION, FOR SIGNAL-DERIVED SHARPNESS-BASED AXIAL LOCALIZATION, USING DIFFERENT TRANSMITTING APERTURES

Transmitting aperture	$Z_{0.5}$ accuracy
Plane Wave (unfocused)	1.84 ± 1.54 μm
Spherical Wave (unfocused)	1.99 ± 1.42 μm
Transmit Focus at 30 mm (focused)	1.87 ± 1.43 μm
Transmit Focus at 40 mm (focused)	1.94 ± 1.86 μm
Transmit Focus at 50 mm (focused)	2.21 ± 1.71 μm

In Fig. 7(a) all curves are slightly skewed, with the edges of the left sides (closer to the transducer surface) slightly shifted to larger values. This is due to the transmit focus being placed closer to the transducer surface. In addition the right sides of the first two *S*-curves presented increased variability compared to the unfocused transmissions (Fig 3). However, as the *S*-curve edges are excluded from the $Z_{0.5}$ calculation, the average d_{dev} (1.87 ± 1.43 μm or $< 0.01\lambda$) was similar to these obtained by using plane or spherical waves. In Fig. 7(b), the transmit focus was placed at 40 mm which is the centre of the investigated range. As a result, the middle *S*-curve (receive focus also at 40 mm) peaked at a higher sharpness value compared to the other two, which increased the rate of sharpness change for that curve. Here, the resulting *S*-curves were symmetric, however variability around the peak areas was visible. The extreme *S*-curves had slightly more flattened peaks which corresponded to reduced rate of sharpness change in these areas. All these resulted to a slightly increased d_{SD} equal to ± 1.86 μm, compared to the PW example ($d_{SD} = \pm 1.54$ μm), while a similar average d_{dev} was acquired (Table II). In Fig. 7(c) as opposed to Fig. 7(a), the edges of the right sides (at greater depths) of the three *S*-curves were slightly shifted to larger values. This was due to the transmit focus effect which was positioned at a greater depth (50 mm) in this instance. The $Z_{0.5}$ did not include the *S*-curve edges as well, hence the average d_{dev} was 2.21 ± 1.71 μm (or $\approx 0.01\lambda$), which was not significantly different from others displayed in Table II. Note that setting the focus further away from the scatterer displacement range (between 32.5 and

This article has been accepted for publication in a future issue of this journal, but has not been fully edited. Content may change prior to final publication. Citation information: DOI 10.1109/ACCESS.2018.2889425, IEEE Access

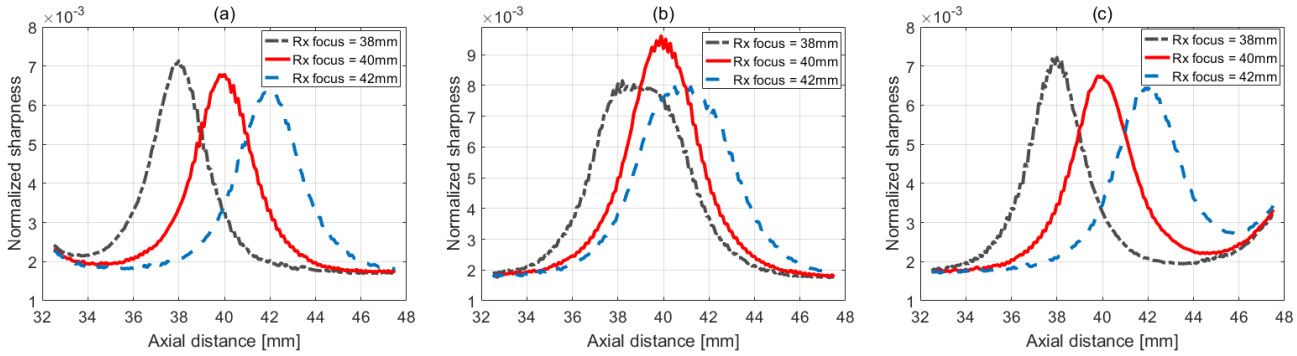

Fig. 7. Normalized sharpness as a function of axial displacement. Different sets of 3 signal-derived *S*-curves are displayed where the ultrasound data were acquired by focused transmission using a fixed transmit focus at depths of a) 30 mm, b) 40 mm, and c) 50 mm respectively. The receive processing is the same for all shown sharpness datasets.

47.5 mm) is in principle closer to that of the PW transmission, which is a focus to infinity.

D. Comparison with Centre of Mass

Table III shows the accuracy in the simulated scatterer axial localization based on both image- and signal-derived sharpness values as well as based on the calculation of the COM for $Z_{0.5}$, $Z_{4\delta_z}$, and $Z_{\sqrt{2}}$. The PW data were used in this study. The image-derived sharpness processing resulted in an average depth deviation to actual simulated scatterer position (d_{dev}) that varied between 17.75 ± 15.67 μm ($\approx 0.08\lambda$) and 18.13 ± 16.55 μm ($\approx 0.08\lambda$) for the 3 ranges. There were no significant differences between the three types of average d_{dev} measurement.

TABLE III
AVERAGE DEPTH DEVIATION TO TRUE SCATTERER POSITION AND ITS STANDARD DEVIATION, FOR SHARPNESS AND COM-BASED AXIAL LOCALIZATION, AND FOR DIFFERENT DEPTH RANGES

Depth range	Image-derived sharpness	Signal-derived sharpness	COM
$Z_{0.5}$	18.13 ± 16.55 μm	1.84 ± 1.54 μm	9.78 ± 4.90 μm
$Z_{4\delta_z}$	17.75 ± 15.67 μm	2.11 ± 1.80 μm	9.86 ± 4.95 μm
$Z_{\sqrt{2}}$	18.16 ± 15.83 μm	2.02 ± 1.73 μm	9.79 ± 4.92 μm

These metrics were improved by a factor of between 9-10 for the signal derived sharpness processing. The average d_{dev} dropped to ≈ 2 μm for all depth ranges as shown in Table III. The COM based axial localization resulted in a constant average d_{dev} equal to ≈ 9.8 μm (or $\approx 0.04\lambda$) for the 3 depth ranges studied here. The corresponding d_{SD} was ± 4.9 μm, for all depth ranges. These numbers were equivalent to at least a 2-fold improvement compared to the image sharpness processing. However, the COM based axial localization was outperformed by the signal derived sharpness processing by a factor of ≈ 5. A high intensity threshold of 0.9 was employed to achieve the results displayed in Table III, and the COM calculation was found to be threshold dependent. For instance, reducing the intensity threshold to 0.7 resulted in average d_{dev} in the range of 20 μm (or $\approx 0.09\lambda$), and the d_{dev} can be significantly worse than that achieved by the image-derived sharpness localization reaching values as high as 40 μm (or $\approx 0.18\lambda$) for intensity thresholds around 0.5.

On the other hand, the COM calculation is independent from the multiple receive processing and partly unrelated to sharpness change. Therefore the entire displacement range (15 mm) is usable for COM-derived axial localization, while the optimized sharpness-based localization here used sub-ranges such as $Z_{0.5}$, $Z_{4\delta_z}$, and $Z_{\sqrt{2}}$. Fig. 8 shows, for clarity, a smoothed version of the 151 (section II-C) individual d_{dev} plotted all together over depth for the three axial localization methods examined here. In general, COM has provided a monotonic improvement of accuracy with depth attributed to the PW transmission. However, the sharpness-based measurement can be optimized to secure a low average d_{dev} in any given depth. For example the result for $Z_{4\delta_z}$ (range between 36 mm-44 mm) can be reproduced for any depths of interest if the equivalent sharpness data are generated.

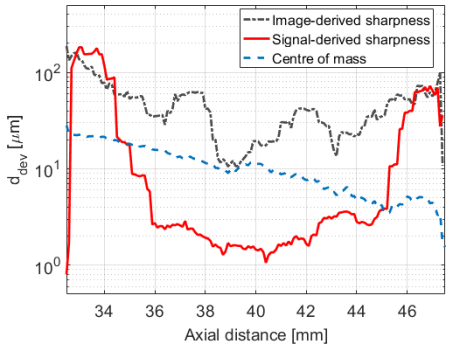

Fig. 8. Simulated depth deviation from scatterer position (d_{dev}) plotted over axial distance for image- and signal-derived sharpness-based axial localization. The equivalent result of COM-based axial localization is also included.

Fig. 9 shows how the individual d_{dev} values relate to the sharpness standard deviation and to the measured FWHM from the PDF [14]. Fig. 9(a) includes a subset of Fig. 6(b), that refers to SNR= 10 dB, and shows that most data points (71.5%) were located in the d_{dev} range between 1 μm and 10 μm and in the sharpness SD range between 0.5×10^{-5} and 4×10^{-5}. This demonstrates that although there is no strong dependence, between the two variables, there is a relative consistency in the value range. Note that the figure here also includes values out-with the $Z_{0.5}$ range in order to observe possible trends for the entire displacement range. Fig. 9(b) shows that the PDF FWHM had a linear relation

This article has been accepted for publication in a future issue of this journal, but has not been fully edited. Content may change prior to final publication. Citation information: DOI 10.1109/ACCESS.2018.2889425, IEEE Access

to d_{dev} ($y = 0.94x + 9.8$, correlation coefficient $r = 0.53$). The result indicates that the width of the PDF can be a reasonable approximation to d_{dev} for each particular depth estimate.

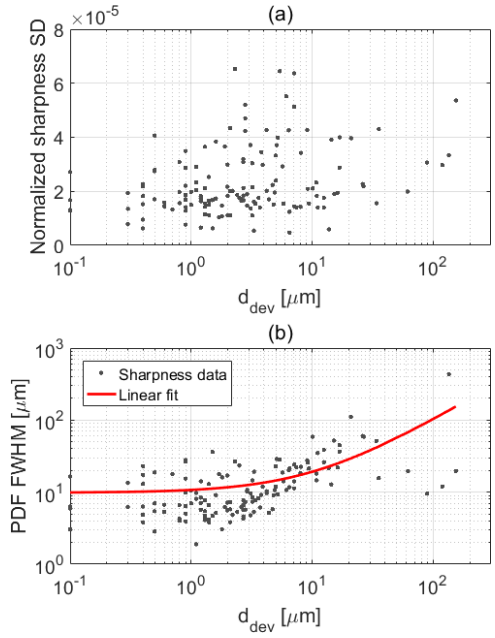

Fig. 9. (a) Normalized sharpness SD and (b) PDF FWHM values over the depth deviation to true simulated scatterer position (d_{dev}), using signal-derived sharpness data.

IV. Results: Experiment

The simulation setup provided an optimal setting for the experimental procedure. A PW transmission was used and a 2 mm receive focus separation was implemented for the sharpness methodology, as this was found to be optimal in section III-A. The measured SNR ranged between $10-20$ dB for depths between 32.5 mm and 47.5 mm. Table IV shows the accuracy in the wire-target axial localization for image- and signal-derived sharpness values as well as the COM calculation for all 3 range type measurements. Overall, the average d_{dev} values were slightly but not significantly increased compared to the simulations. The image-derived sharpness processing resulted in an average d_{dev} that varied between 22.16 ± 17.27 μm (or $\approx 0.10\lambda$) and 26.30 ± 22.71 μm (or $\approx 0.12\lambda$) for the 3 depth ranges.

TABLE IV
Average Depth Deviation to True Wire Position and its Standard Deviation, for Sharpness and COM-based Axial Localization, and for Different Depth Ranges

Depth range	Image-derived sharpness	Signal-derived sharpness	COM
$Z_{0.5}$	22.16 ± 17.27 μm	2.30 ± 1.83 μm	13.30 ± 6.74 μm
$Z_{4\delta_z}$	25.77 ± 22.64 μm	2.61 ± 2.12 μm	14.04 ± 8.13 μm
$Z_{\sqrt{2}}$	26.30 ± 22.71 μm	2.59 ± 2.12 μm	14.19 ± 8.18 μm

The above figures were improved by a factor of ≈ 10 for the signal derived sharpness processing. The average d_{dev} varied to between 2.30 ± 1.83 μm and 2.61 ± 2.12 μm (or $\approx 0.01\lambda$) for all depth ranges. The COM provided a d_{dev} that ranged between 13.30 ± 6.74 μm (or $\approx 0.06\lambda$) and 14.19 ± 8.18 μm (or $\approx 0.07\lambda$). These numbers were an almost 2-fold improvement compared to those provided by the image-based sharpness. On the other hand, the COM based axial localization was outperformed by the signal-derived sharpness processing by a factor of at least 5. An intensity threshold of 0.7 was employed to achieve the results displayed in Table IV in the wire-target experiment, and the COM calculation was found to be threshold dependent. Increasing or reducing the intensity threshold resulted in reduced localization accuracy. Higher average d_{dev} values were measured and the uncertainty in the localization reached values up to 44 μm (or $\approx 0.21\lambda$). These values were worse compared not only to the signal-derived sharpness processing but also to the image-derived one. These results compare well with the simulation.

Fig. 10(a) shows an image of the wire-target, from the experimentally acquired data which resembles to the simulated ones displayed in Fig. 5, and rather closest to Fig. 5(c) given the noise level. Fig. 10(b) is a visual display of the "trimming" result achieved axially by the image-derived sharpness to the PSF. Fig. 10(c) shows the equivalent results achieved by the signal-derived sharpness processing and the COM calculation. The normalized sharpness processing is related to the localization in the axial direction only and has no effect on the lateral direction, unlike the COM which provides a localization in both directions.

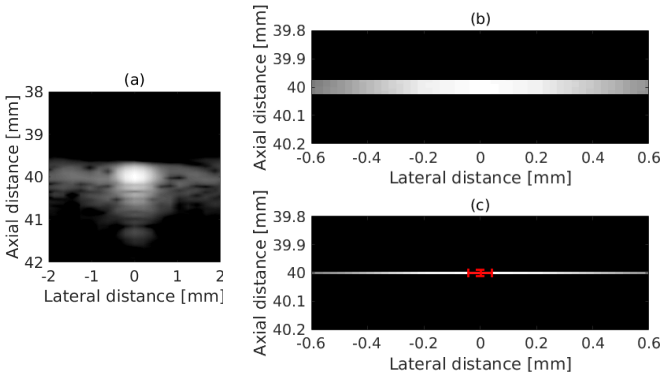

Fig. 10. (a) Example of an experimentally acquired PSF. The wire-target and the receive focus were positioned at 40 mm depth. A 60 dB dynamic range display was used. Visualization of (b) image-derived sharpness and (c) signal-derived sharpness (white) and centre of mass axial localization (red) for the PSF displayed in (a) using the average values shown in Table IV.

Fig. 11 shows a smoothed version of the 139 (section II-D) individual d_{dev} plotted over depth for the three axial localization methods. Similarly to the simulations, the COM provided a monotonic improvement of accuracy with depth. Fig. 12 shows how the d_{dev} values relate to the sharpness standard deviation and to the measured FWHM from the PDF, for the experimentally acquired point scatterer data. The figure directly compares with the Fig. 9, which includes the simulated data. Fig. 12(a) shows that 65.7% of the data points were concentrated in the area defined by d_{dev} values between 1 μm and 10 μm and by sharpness SD values between 1×10^{-5} and 4×10^{-5} which is a fairly similar behaviour compared to that noted in Fig. 9(a) for the simulated scatterer. In general, the sharpness SD was kept below 4.5×10^{-5} during the

This article has been accepted for publication in a future issue of this journal, but has not been fully edited. Content may change prior to final publication. Citation information: DOI 10.1109/ACCESS.2018.2889425, IEEE Access

experiment. Fig. 9(b) shows that the PDF FWHM variation had a linear relation to d_{dev} ($y = 1.3x + 12$, $r = 0.59$). The linear function and the measured correlation coefficient were not significantly different from these found for the simulated data (section III-D).

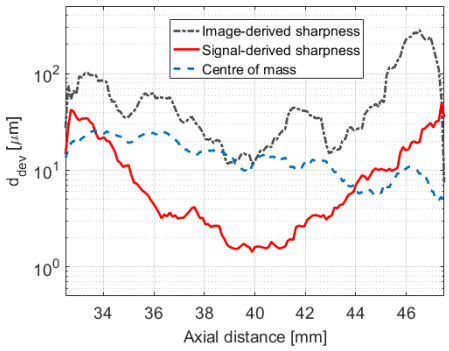

Fig. 11. Depth deviation to true wire-target position (d_{dev}) plotted over axial distance for image- and signal-derived sharpness-based axial localization. The equivalent result of COM-based axial localization is also included.

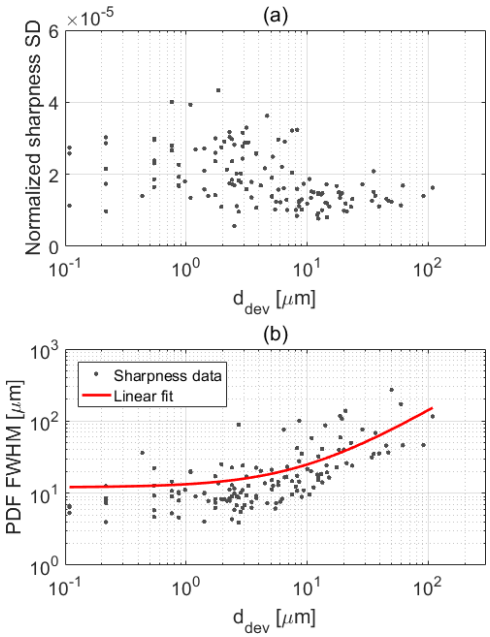

Fig. 12. (a) Normalized sharpness standard deviation and (b) PDF FWHM values over the depth deviation to true wire-target position (d_{dev}), using signal-derived sharpness data.

V. Discussion

The sharpness-based method originally presented in [14] as an alternative for the precise axial localization of ultrasound point scatterers, was further developed in this work, using implementation and imaging parameters that cover a range of possible imaging scenarios. The sharpness methodology provided consistently an axial localization precision (≈ 2 μm) at least 2 orders of magnitude lower than the wavelength used (220 μm), which is an indication of the system's resolution, over different SNRs, transmission and receive settings. Under high SNR conditions the localization precision may be over 3 orders of magnitude lower than the wavelength. The data analysis showed that in areas dominated by two of the *S*-curve slopes, thus excluding the edges of the 15 mm total axial displacement, the normalized sharpness method performs best, achieving axial localization accuracy which outperforms that displayed previously by a factor of ≈ 5 [14]. Fundamental to the optimization process here is the understanding on how the *S*-curves can be used more efficiently. As stated previously, the best localization is achieved where the *S*-curves present a sharp change with depth, which is the area of sharp defocus next to the focus. On the other hand, the areas of low sharpness values where also sharpness changes very little with depth, result in an increased error in the axial localization. The three different types of ranges ($Z_{0.5}$, $Z_{4\delta z}$, $Z_{\sqrt{2}}$) used did not provide significantly different results, as they do not incorporate low sharpness values. Further good agreement was achieved between experimental results and simulations. The experimental results provided an average depth deviation to true scatterer position of ≈ 25 μm and ≈ 2.5 μm (Table IV) for image- and signal-derived sharpness respectively, while the simulations provided respective figures of ≈ 18 μm and ≈ 2 μm (Table III). The 9- to 10-fold improvement in axial localization accuracy was an expected result and agrees with the previous work [14]. The image formation includes compression, interpolation, time-gain compensation and display conversion which leads to significant loss of information.

Therefore, the signal-derived sharpness processing was also expected to provide superior axial localization compared to the COM localization, and the improvement was approximately 5-fold in the experiment. In general, the COM calculations (between 10 μm and 14 μm) here compare well with others found in the literature that were between 10 μm and 20 μm at best [5]–[7], [32], and corresponded to localization improvements between 5- and 25-fold compared to the wavelengths used. Axial localization with improved precision of 1.9 μm ($f_0 =$ 3 MHz, $\lambda =$ 500 μm) has recently been achieved [33], but in this work two transducers positioned orthogonally to each other were used, which resulted in an increased aperture. In Figs. 8 and 11 the COM measurement is relatively stable for the entire image, while, as mentioned above, the sharpness-derived localization is best well within the range of the *S*-curves. However, this is not a limiting factor as the number of curves can be extended to cover the desired axial range in the image. Further, the COM estimation is dependent on the intensity threshold applied to the images before its estimation. In this study the PSF had a regular and symmetric shape, which led to the optimal choice of threshold that produced optimal COM results. This may not be the case for real imaging conditions where scatterers may appear to have irregular shape and intensity profile. Nonetheless, the COM remains a very good practical solution for image-based measurement, providing a scatterer centre in both dimensions of the image.

While the PSF can be significantly affected by speed of sound and attenuation variations, the proposed method is independent of such variations and is only linked to the sharpness metric. The general Lorentzian-like shape of the *S*-curve was preserved throughout the present study as seen in Figs. 3

and 7, which resulted in similar order of localization accuracy. Further work with actual MB scatterers in *in-vivo* settings, will involve the presence of isolated scattering events as in all super-resolution methods. The precise estimation of a depth position will be achieved by assessing multiple sharpness values and by matching these values to an existing set of calibration data. These data might stem from a simple *in-vitro* (for instance a wire-target) experiment using the same imaging protocol prior to the *in-vivo* scan, or one of the simulated *S*-curve sets that have been generated in this work might be directly employed, depending on the imaging conditions. Hence, the study performed here with the simulated data and the controlled experimental setup allows to determine the exact capabilities and the limits of the normalized sharpness method for real imaging scenarios as well. A potential MB application would also require the control of the contrast agent density in an image, since each sharpness value must be evaluated only from a small area around a single PSF. This is because with this restriction, the aberrations including (and dominated by) the focus errors are well-defined, symmetric and can be contained within a single analysis frame, as explained in [17].

Importantly, the connection of the localization accuracy with metrics such as the sharpness standard deviation (SD) or the full-width-at-half-maximum (FWHM) of the probability density function (PDF) suggests that the normalized sharpness method may be deployed without the "true scatterer position" requirement for the generation of the calibration data. The true scatterer position may be precisely known when performing experimental measurements using for example a high-precision translation stage. By contrast, such knowledge is not attainable in a real imaging scenario. Figs. 9(b) and 12(b) confirmed that the calculated FWHM of the PDF correlates with the measured d_{dev} values, and their value ranges were very similar. Thus, the comparison of a depth estimate with the true scatterer position may be substituted by the FWHM of the PDF, or by the sharpness SD obtained from the repetitive measurements. Such measurements would perhaps require longer raw ultrasound data acquisitions, which are feasible for most real imaging scenarios.

In general, the power of the technique lies in the measurement of the PSF without the requirement to assume a PSF model, and in the fact that it is robust in changes of noise, transmission protocol and flexible in terms of receive focus protocol. The sharpness technique also proved to perform equally well with all common types of ultrasound transmission. The focused transmission is commonly employed in state-of-the-art ultrasound. The other two transmission types have the ability to produce single emission images thus enabling a high frame rate, but at the same time result in lower resolution compared to focused transmission. However, a number of emissions may be used to further enhance the imaging resolution, either by using synthetic aperture imaging [28], or by applying compounding which is the transmission of multiple plane waves at different angles [34]. An important parameter in the choice of contrast enhanced ultrasound imaging, as mentioned in the introduction, is the acoustic pressure field and the microbubble sensitivity across the image. In the light of this, it may be that a single emission protocol will favour smaller region of interest investigations, while the focused transmission may enable entire organ visualization.

The normalized sharpness method, similar to the techniques related to the lateral [35] or frequency [36] resolution, may add to the existing super-resolution methods. Current super-resolution ultrasound is heavily based on image processing. It has been accomplished either by identifying the PSF COM [6], [7] or by fitting three dimensional Gaussian functions [12], [13] to ultrasound reconstructed data to approximate the PSF. Note that both methods provide similar results and are dependent on the SNR. The possibility to enhance the point scatterer localization is reliant on exploiting the otherwise lost detail from the raw ultrasound data, when converting them to images. The sharpness method although limited to the axial direction, may be considered as a signal-based adjunct to the already existing image-based methods. The work here suggests that a combination of the COM (for the lateral direction) with the sharpness method (for the axial direction) will provide the most accurate scatterer location. The ultimate objective is the expansion of the sharpness method to the estimation of all three co-ordinates of a point source such as MBs. Ultrasound scanning with modern $2D$ array probes could be explored to extract sharpness values that will correspond to a total position instead of just a z-position.

VI. Conclusion

Different approaches of the normalized sharpness method were examined under various imaging conditions. The method exploits the defocus aberrations to achieve axial localization of ultrasound point scatterers with super-resolution accuracy of a few microns. The approaches involved different foci separation in the receive processing of the raw ultrasound point scatterer data, and subsequently the calculation of the sharpness metric based on both signal and image data. The imaging conditions included different types of ultrasound transmission as well as different amounts of noise added to the ultrasound data. The results showed that an axial localization precision of between $2-6$ μm can be achieved using the signal data. From the above precision range, the lower limit is equivalent to a ≈ 5-fold improvement in axial localization precision compared to that achieved by using the centre of mass (COM) method. The upper limit which is closer to COM (≈ 10 μm), is related to highly noisy data. Overall, this work highlights the benefits of signal compared to image processing and provides results which may be significant when reconstructing microvessels of the order of tens of micrometres in diameter.

References

[1] S. T. Hess, T. P. K. Girirajan, and M. D. Mason, "Ultra-high resolution imaging by fluorescence photoactivation localization microscopy," *Biophys. J.*, vol. 91, no. 11, pp. 4258–4272, 2006.

[2] E. Betzig, G. H. Patterson, R. Sougrat, O. W. Lindwasser, S. Olenych, J. S. Bonifacino, M. W. Davidson, J. Lippincott-Schwartz, and H. F. Hess, "Imaging intracellular fluorescent proteins at nanometer resolution," *Science*, vol. 313, no. 5793, pp. 1642–1645, 2006.

[3] M. Bates, B. Huang, G. T. Dempsey, and X. Zhuang, "Multicolor super-resolution imaging with photo-switchable fluorescent probes," *Science*, vol. 317, no. 5845, pp. 1749–1753, 2007.

[4] M. A. O'Reilly and K. Hynynen, "A super-resolution ultrasound method for brain vascular mapping," *Med. Phys.*, vol. 40, no. 11, p. 110701, 2013.

[5] M. A. O'Reilly, R. M. Jones, and K. Hynynen, "Three-dimensional transcranial ultrasound imaging of microbubble clouds using a sparse hemispherical array," *IEEE Trans. Biom. Eng.*, vol. 61, no. 4, pp. 1285–1294, 2014.

[6] K. Christensen-Jeffries, R. J. Browning, M. X. Tang, C. Dunsby, and R. J. Eckersley, "*In vivo* acoustic super-resolution and super-resolved velocity mapping using microbubbles," *IEEE Trans. Medical Imaging*, vol. 34, no. 2, pp. 433–440, Feb. 2015.

[7] C. Errico, B. F. Osmanski, S. Pezet, O. Couture, Z. Lenkei, and M. Tanter, "Transcranial functional ultrasound imaging of the brain using microbubble-enhanced ultrasensitive doppler," *NeuroImage*, vol. 124, no. Pt A, pp. 752–761, 2015.

[8] C. Errico, J. Pierre, S. Pezet, Y. Desailly, Z. Lenkei, O. Couture, and M. Tanter, "Ultrafast ultrasound localization microscopy for deep super-resolution vascular imaging," *Nature letter*, vol. 527, no. 7579, pp. 499–502, 2015.

[9] O. Couture, V. Hingot, B. Heiles, P. Muleki-Seya, and M. Tanter, "Ultrasound localization microscopy and super-resolution:A state of the art," *IEEE Trans. Ultrason., Ferroelectr., Freq. Control*, vol. 65, no. 8, pp. 1304–1320, Aug. 2018.

[10] Y. Desailly, O. Couture, M. Fink, and M. Tanter, "Sono-activated ultrasound localization microscopy," *Appl. Phys. Lett.*, vol. 103, no. 17, p. 174107, 2013.

[11] Y. Desailly, J. Pierre, O. Couture, and M. Tanter, "Resolution limits of ultrafast ultrasound localization microscopy," *Phys. Med. Biol.*, vol. 60, no. 22, pp. 8723–8740, 2015.

[12] K. Christensen-Jeffries, S. Harput, J. Brown, P. N. T. Wells, P. Aljabar, C. Dunsby, M. X. Tang, and R. J. Eckersley, "Microbubble axial localization errors in ultrasound super-resolution imaging," *IEEE Trans. Ultrason., Ferroelectr., Freq. Control*, vol. 64, no. 11, pp. 1644–1654, Nov. 2017.

[13] P. Song, A. Manduca, J. D. Trzasko, R. E. Daigle, and S. Chen, "On the effects of spatial sampling quantization in super-resolution ultrasound microvessel imaging," *IEEE Trans. Ultrason., Ferroelectr., Freq. Control*, pp. 1–1, 2018.

[14] K. Diamantis, A. Greenaway, T. Anderson, J. Jensen, P. Dalgarno, and V. Sboros, "Super-resolution axial localization of ultrasound scatter using multi-focal imaging," *IEEE Trans. Biomed. Eng.*, vol. 65, no. 8, pp. 1840–1851, July 2018.

[15] M. Tanter and M. Fink, "Ultrafast imaging in biomedical ultrasound," *IEEE Trans. Ultrason., Ferroelec., Freq. Contr.*, vol. 61, no. 1, pp. 102–119, 2014.

[16] P. A. Dalgarno, H. I. C. Dalgarno, A. Putoud, R. Lambert, L. Paterson, D. C. Logan, D. P. Towers, R. J. Warbuton, and A. H. Greenaway, "Multiplane imaging and three dimensional nanoscale particle tracking in biological microscopy," *Opt. Expr.*, vol. 18, no. 2, pp. 877–884, 2010.

[17] H. I. C. Dalgarno, P. A. Dalgarno, A. C. Dada, G. J. G. C. E. Towers, R. M. Parton, I. Davis, R. J. Warburton, and A. H. Greenaway, "Nanometric depth resolution from multi-focal images in microscopy," *J. R. Soc. Interface*, vol. 8, no. 60, pp. 942–951, July 2011.

[18] V. Sboros, C. M. Moran, S. D. Pye, and W. N. McDicken, "The behaviour of individual contrast agent microbubbles," *Ultr. Med. Biol.*, vol. 29, no. 5, pp. 687–694, 2003.

[19] V. Sboros, "Response of contrast agents to ultrasound," *Adv. Drug Deliv. Rev.*, vol. 60, no. 10, pp. 1117–1136, June 2008.

[20] J. A. Jensen and N. B. Svendsen, "Calculation of pressure fields from arbitrarily shaped, apodized, and excited ultrasound transducers," *IEEE Trans. Ultrason., Ferroelectr., Freq. Control*, vol. 39, pp. 262–267, 1992.

[21] J. A. Jensen, "Field: A program for simulating ultrasound systems," *Med. Biol. Eng. Comp., vol. 10th Nordic-Baltic Conference on Biomedical Imaging, Supplement 1, Part 1*, vol. 4, pp. 351–353, 1996.

[22] R. A. Muller and A. Buffington, "Real-time correction of atmospherically degraded telescope images through image sharpnening," *J. Opt. Soc. Am.*, vol. 64, no. 9, pp. 1200–1210, Sep. 1974.

[23] M. Subbarao and J.-K. Tyan, "Selecting the optimal focus measure for autofocusing and depth-from-focus," *IEEE Trans. on Pattern Analysis and Machine Intelligence*, vol. 20, no. 8, pp. 864–870, 1998.

[24] N. K. Chern, P. A. Neow, and M. H. A. Jr., "Practical issues in pixel-based auto focusing for machine vision," in *Proc. IEEE Robotics and Automation*, May 2001, pp. 2791–2796.

[25] K. Diamantis, P. A. Dalgarno, A. H. Greenaway, T. Anderson, J. A. Jensen, and V. Sboros, "High resolution depth-resolved imaging from multi-focal images for medical ultrasound," in *Proc. IEEE Eng. in Med. and Biol. Soc.*, 2015, pp. 7067–7070.

[26] ——, "A novel array processing method for precise depth detection of ultrasound point scatter," in *Proc. IEEE Int. Conf. Acous., Speech, Sig. Pro. (ICASSP)*, 2016, pp. 669–673.

[27] K. Diamantis, I. H. Voxen, A. H. Greenaway, T. Anderson, J. A. Jensen, and V. Sboros, "A comparison between temporal and subband minimum variance adaptive beamforming," in *Proc. SPIE Med. Imag.*, vol. 90400L, Mar. 2014. [Online]. Available: 10.1117/12.2043602.

[28] S. I. Nikolov and J. A. Jensen, "In-vivo synthetic aperture flow imaging in medical ultrasound," *IEEE Trans. Ultrason., Ferroelectr., Freq. Control*, vol. 50, no. 7, pp. 848–856, 2003.

[29] W. Marczak, "Water as a standard in the measurements of speed of sound in liquids," *J. Acoust. Soc. Am.*, vol. 102, no. 5, pp. 2776–2779, 1997.

[30] J. A. Jensen, H. Holten-Lund, R. T. Nilsson, M. Hansen, U. D. Larsen, R. P. Domsten, B. G. Tomov, M. B. Stuart, S. I. Nikolov, M. J. Pihl, Y. Du, J. H. Rasmussen, and M. F. Rasmussen, "Sarus: A synthetic aperture real-time ultrasound system," *IEEE Trans. Ultrason., Ferroelectr., Freq. Control*, vol. 60, no. 9, pp. 1838–1852, 2013.

[31] J. M. Hansen, M. C. Hemmsen, and J. A. Jensen, "An object-oriented multi-threaded software beam formation toolbox," in *Proc. SPIE Med. Imag.*, vol. 79680Y, Mar. 2011. [Online]. Available: 10.1117/12.878178.

[32] D. Ackermann and G. Schmitz, "Detection and tracking of multiple microbubbles in ultrasound b-mode images," *IEEE Trans. Ultrason., Ferroelec., Freq. Contr.*, vol. 63, no. 1, pp. 72–82, Jan. 2016.

[33] K. Christensen-Jeffries, J. Brown, P. Aljabar, M. Tang, C. Dunsby, and R. J. Eckersley, "3-D in vitro acoustic super-resolution and super-resolved velocity mapping using microbubbles," *IEEE Trans. Ultrason., Ferroelectr., Freq. Control*, vol. 64, no. 10, pp. 1478–1486, Oct. 2017.

[34] G. Montaldo, M. Tanter, J. Bercoff, N. Benech, and M. Fink, "Coherent plane-wave compounding for very high frame rate ultrasonography and transient elastography," *IEEE Trans. Ultrason., Ferroelectr., Freq. Control*, vol. 56, no. 3, pp. 489–506, Mar. 2009.

[35] K. Diamantis, A. Greenaway, T. Anderson, J. A. Jensen, and V. Sboros, "Experimental performance assessment of the sub-band minimum variance beamformer for ultrasound imaging," *Ultrasonics*, vol. 79, pp. 87–95, 2017.

[36] K. Diamantis, A. Dermitzakis, J. R. Hopgood, and V. Sboros, "Super-resolved ultrasound echo spectra with simultaneous localization using parametric statistical estimation," *IEEE Access*, vol. 6, pp. 14 188–14 203, 2018.